



Tidal Inflation Reconciles Low-density Sub-Saturns with Core Accretion

Sarah Millholland^{1,4} , Erik Petigura² , and Konstantin Batygin³ 

¹ Department of Astronomy, Yale University, New Haven, CT 06511, USA; sarah.millholland@yale.edu

² Department of Physics & Astronomy, University of California Los Angeles, Los Angeles, CA 90095, USA

³ Division of Geological and Planetary Sciences, California Institute of Technology, Pasadena CA 91125, USA

Received 2020 March 20; revised 2020 May 11; accepted 2020 May 20; published 2020 June 26

Abstract

While the solar system contains no planets between the sizes of Uranus and Saturn, our current exoplanet census includes several dozen such planets with well-measured masses and radii. These sub-Saturns exhibit a diversity of bulk densities, ranging from ~ 0.1 to 3 g cm^{-3} . When modeled simply as hydrogen/helium envelopes atop rocky cores, this diversity in densities translates to a diversity in planetary envelope fractions, $f_{\text{env}} = M_{\text{env}}/M_p$, ranging from $\sim 10\%$ to $\sim 50\%$. Planets with $f_{\text{env}} \approx 50\%$ pose a challenge to traditional models of giant planet formation by core-nucleated accretion, which predict the onset of runaway gas accretion when $M_{\text{env}} \sim M_{\text{core}}$. Here, we show that many of these apparent $f_{\text{env}} \approx 50\%$ planets are less envelope-rich than they seem, after accounting for tidal heating. We present a new framework for modeling sub-Saturn interiors that incorporates envelope inflation due to tides, which are driven by the observed nonzero eccentricities, as well as potential obliquities. Consequently, when we apply our models to known sub-Saturns, we infer lower f_{env} than tides-free estimates. We present a case study of K2-19 b, a moderately eccentric sub-Saturn. Neglecting tides, K2-19 b appears to have $f_{\text{env}} \approx 50\%$, poised precariously near the runaway threshold; by including tides, however, we find $f_{\text{env}} \approx 10\%$, resolving the tension. Through a systematic analysis of $4\text{--}8 R_{\oplus}$ planets, we find that most (but not all) of the similarly envelope-rich planets have more modest envelopes of $f_{\text{env}} \approx 10\text{--}20\%$. Thus, many sub-Saturns may be understood as sub-Neptunes that have undergone significant radius inflation, rather than a separate class of objects. Tidally induced radius inflation likely plays an important role in other size classes of planets including ultra-low-density Jupiter-size planets like WASP-107 b.

Unified Astronomy Thesaurus concepts: Exoplanets (498); Extrasolar gas giants (509); Exoplanet atmospheres (487); Exoplanet structure (495); Exoplanet tides (497)

1. Introduction

Extrasolar systems harbor many planets with no solar system analog. The solar system is devoid of planets with radii between those of Earth and Neptune ($3.9 R_{\oplus}$), yet this is the most prevalent extrasolar class size known (Howard et al. 2012; Dressing & Charbonneau 2013; Fressin et al. 2013; Petigura et al. 2013). It also lacks planets with sizes between Uranus ($4.0 R_{\oplus}$) and Saturn ($9.4 R_{\oplus}$). These sub-Saturns, which we define as in previous works to be planets in the range $4.0\text{--}8.0 R_{\oplus}$ (Petigura et al. 2017b), are less common than sub-Neptunes but are still found within $P < 300$ days around $\sim 7\%$ of Sun-like stars (Petigura et al. 2018b; Hsu et al. 2019). The lack of local analogues for these short-period exoplanets results in many mysteries about their interior structures, formation, and evolution. One such example is found in the population of sub-Saturns.

The low densities of sub-Saturns imply that they must have substantial atmospheric envelopes (Rogers & Seager 2010; Rogers 2015; Wolfgang & Lopez 2015). Their composition is likely a heavy element core of rocky material, surrounded by a gaseous envelope dominated by hydrogen and helium (Marcy et al. 2014; Weiss & Marcy 2014; Rogers 2015). Sub-Saturns as a population exhibit significant scatter in their mass–radius relationship (Petigura et al. 2017b).

The observed masses and radii may be converted into interior structure constraints by employing core-envelope models. Lopez & Fortney (2014) constructed model planets consisting of Earth-composition cores surrounded by low-density envelopes of H/He.

Considering a grid of M_{core} , M_{env} , age, and incident stellar flux, they computed the planetary radius evolution in response to various sources of envelope heating and cooling.⁵ Critically, given these assumptions, one may invert these models and translate the masses and radii of observed planets into constraints on their core and envelope masses.

Using this approach, there has emerged a subset of low-density sub-Saturns with atmospheric envelopes comprising $\sim 50\%$ of their total mass. (That is, their envelope mass fractions are $f_{\text{env}} \equiv M_{\text{env}}/M_p \approx 50\%$.) Examples of such planets, which are perplexing for reasons we will describe below, include the recently discovered K2-24 c (Petigura et al. 2018a) and K2-19 b (Petigura et al. 2020). Both planets are found near or in mean-motion resonances (MMRs) with neighboring companions and have nonzero eccentricities, $e \sim 0.08$ for K2-24 c and $e \sim 0.2$ for K2-19 b. Using the Lopez & Fortney (2014) models, Petigura et al. (2018a) estimated that K2-24 c required an envelope mass fraction equal to $f_{\text{env}} = 52^{+5}_{-3}\%$, while K2-19 b was inferred to have $f_{\text{env}} = 44\% \pm 3\%$ (Petigura et al. 2020).

These near-50% envelope mass fraction planets are puzzling because they should be rare according to the theory of core accretion, which represents the dominant paradigm of planet formation for gas-rich planets (e.g., Mizuno 1980; Stevenson 1982; Pollack et al. 1996). Core accretion theory

⁵ These sources include cooling of the atmosphere through radiation, cooling of the core (which delays the envelope cooling/contraction), and heating from radioactive decay. Within the framework of these standard models, the planet radius is an effective proxy for the envelope mass fraction (e.g., Lopez & Fortney 2014; Chen & Rogers 2016).

⁴ NSF Graduate Research Fellow.

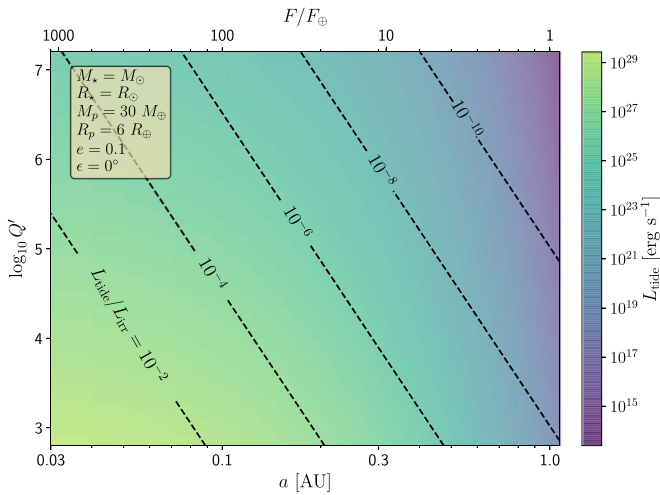


Figure 1. Magnitude of the tidal luminosity, L_{tide} (Equation (1)), as a function of $\log_{10} Q'$ and a (bottom x -axis) or F/F_{\odot} (top x -axis). We assume fiducial sub-Saturn system parameters, which are shown in the top left. Contours are lines of constant $L_{\text{tide}}/L_{\text{irr}}$, where L_{irr} is the incident stellar power.

holds that solid cores that form before the dissipation of the protoplanetary disk will accrete gas at a rate set by their internal cooling (e.g., Lee & Chiang 2015; Ginzburg et al. 2016). When the mass in the envelope reaches a threshold approximately equal to the core mass, the envelope will hydrodynamically collapse under its own self-gravity and undergo a phase of runaway gas accretion at a rate limited by the accretionary mass flux (Hubickyj et al. 2005; Batygin et al. 2016).

While, for an individual planet, one cannot rule out that the protoplanetary disk disappeared at the same instant that the growing envelope mass reached the core mass, such fine-tuning suggests this should be rare. Thus, the discovery of planets with these exact properties is in tension with this picture. Moreover, the problem is not just that there are specific cases that are in conflict; for $P < 100$ days, sub-Saturns appear roughly as common as gas giants. That is, the occurrence rate is flat beyond $\sim 4 R_{\oplus}$ (Petigura et al. 2018b).

In this paper, we propose that most sub-Saturns are not as gas-rich as their masses and radii would suggest, but rather, their envelopes have been inflated through tidal heating. Sub-Saturns are often found on short-period orbits with moderate eccentricities (Petigura et al. 2017b). Short-period planets experience substantially stronger tidal interactions with their host stars than any of the solar system planets due to a steep inverse distance dependence in the tidal forcing. Tidal heating inevitably arises both from eccentricity tides, which result from the nonuniform tidal forces along the eccentric orbits, and from obliquity tides, which are produced when the planet has a nonzero axial tilt (“obliquity”) of its spin axis relative to its orbital axis. For instance, at 0.1 au, these tidal interactions can result in a tidal luminosity up to $L_{\text{tide}} \sim 10^{29} \text{ erg s}^{-1}$, or roughly $L_{\text{tide}}/L_{\text{irr}} \sim 0.01$, where L_{irr} is the incident stellar power (see Figure 1).

Radius inflation from tidal heating is not a new consideration. It was one of the proposed sources of the extra heating required to explain the distended radii of hot Jupiters, whose sizes are infamously at odds with standard thermal evolution models (e.g., Bodenheimer et al. 2001; Ogilvie & Lin 2004; Jackson et al. 2008; Ibgui & Burrows 2009; Miller et al. 2009). Tidal heating has also been suggested to be important during the formation of super-Earths/sub-Neptunes by inhibiting their

cooling and gas accretion (Ginzburg & Sari 2017). More recently, Millholland (2019), hereafter M19, examined the impacts of tidal heating on the radii of sub-Neptunes. They demonstrated that tides can inflate sub-Neptune radii by up to a factor of two when $L_{\text{tide}}/L_{\text{irr}} \gtrsim 10^{-5}$. In particular, M19 proposed that obliquity tides might explain signatures of radius enhancement of planets wide of first-order MMRs.

Planets with active tidal heating are larger at a fixed f_{env} . Consequently, the inclusion of tidal heating in a structural model will yield smaller f_{env} estimates for observed planets. For instance, M19 presented case studies of some of the ultra-low-density ($\rho \lesssim 0.1 \text{ g cm}^{-3}$) “super-puff” planets (e.g., Jontof-Hutter et al. 2014) and showed that these planets could have $f_{\text{env}} \sim 5\%$ (as opposed to $f_{\text{env}} \gtrsim 30\%$) if tidal heating is active. For short-period orbits, tidal inflation and the associated modifications to the f_{env} estimates are inevitable when the eccentricities and/or obliquities are nonzero.

In this work, we extend the M19 analysis to sub-Saturns by considering planets with larger masses and envelope mass fractions (which were capped in M19 at $20 M_{\oplus}$ and 30%, respectively). We address the question of whether tidal inflation solves the mystery of the apparently anomalous envelope mass fractions, and we study how much tidal inflation impacts the population of sub-Saturns as a whole. We begin with a description of our tidal model, planetary thermal evolution model, and procedure for parameter estimation of observed planets (Section 2). We then present a case study of the K2-19 system (Section 3), which was the original motivation of this work. We expand the analysis to the broader sub-Saturn population in Section 4 and demonstrate that planets across the population are significantly impacted by tidal inflation. In Section 5, we discuss the relationship between sub-Saturns and planets in other class sizes, and we consider implications and predictions of our theory.

2. Methods

To study the impacts of tidal heating on the structures of short-period planets, we employ a thermal evolution model that captures the cooling and contraction of the planetary envelope, while also including heating from tidal dissipation. We have done so by building onto a publicly available sub-Neptune evolutionary model developed by Chen & Rogers (2016). Here, we enumerate our assumptions about tidal dissipation (Section 2.1), our thermal evolution model of planetary structure (Section 2.2), and our model-fitting and error estimation procedure (Section 2.3). Most of these methods were employed in the M19 analysis, and further details may be found therein. Elements of our analysis are available at <https://github.com/smiholland/Sub-Saturns/>; readers can use this code to derive their own planet parameter estimations.

2.1. Tidal Model

Tidal dissipation involves the conversion of orbital energy into thermal energy in an orbiting body due to tidal deformations raised by the primary body. Tides are complex in general, and the details of where, how, and how much energy is dissipated are nontrivial. Here, we choose to model the tidal dissipation using the viscous approach to traditional equilibrium tide theory (e.g., Darwin 1880; Goldreich & Soter 1966; Mignard 1979; Hut 1981). The fundamental assumption is that the planet’s tidal response to the star is an

equilibrium deformation, or tidal bulge, and this bulge lags the star’s position with a constant time offset (Ferraz-Mello et al. 2008; Wisdom 2008; Leconte et al. 2010). The physics of the tidal distortion are effectively encapsulated in the parameter Q' , the “reduced tidal quality factor.” While this parameter is highly uncertain for an individual planet, we consider a broad range of plausible values throughout this analysis.

We note that there are many alternative tidal models that employ different relationships between the tidal forcing frequency and the phase lag angle (e.g., Efroimsky & Williams 2009; Ferraz-Mello 2013; Correia et al. 2014; Storch & Lai 2014; Boué et al. 2016). Here, we are aiming to infer the first-order physical response of tidal heating in sub-Saturn planets, whose specific compositions and rheologies are uncertain. Accordingly, we believe the simplest approach offered by the equilibrium tidal model is an appropriate starting place.

In this framework, the tidal luminosity—or the rate at which orbital energy is converted into heat energy—is given by the following expression from Leconte et al. (2010):

$$L_{\text{tide}}(e, \epsilon) = 2K \left[N_a(e) - \frac{N^2(e)}{\Omega(e)} \frac{2 \cos^2 \epsilon}{1 + \cos^2 \epsilon} \right]. \quad (1)$$

Here, e is the orbital eccentricity, and ϵ is the obliquity—or the angle between the planet’s spin axis and its orbital axis.⁶ We define $N_a(e)$, $N(e)$, $\Omega(e)$ to be functions of eccentricity given by

$$N_a(e) = \frac{1 + \frac{31}{2}e^2 + \frac{255}{8}e^4 + \frac{185}{16}e^6 + \frac{25}{64}e^8}{(1 - e^2)^{\frac{15}{2}}} \quad (2)$$

$$N(e) = \frac{1 + \frac{15}{2}e^2 + \frac{45}{8}e^4 + \frac{5}{16}e^6}{(1 - e^2)^6} \quad (3)$$

$$\Omega(e) = \frac{1 + 3e^2 + \frac{3}{8}e^4}{(1 - e^2)^{\frac{9}{2}}}. \quad (4)$$

The quantity K is the characteristic luminosity scale,

$$K = \frac{3n}{2} \frac{k_2}{Q} \left(\frac{GM_\star}{R_p} \right)^2 \left(\frac{R_p}{a} \right)^6, \quad (5)$$

where $n = 2\pi/P$ is the mean motion, a is the semimajor axis, M_\star is the stellar mass, and R_p is the planet radius. The two parameters k_2 and Q relate to the planet’s composition and interior structure. The parameter k_2 is the dimensionless Love number, and it is connected to the planet’s deformation response to tidal disturbance, as well as the central concentration of the planet’s density profile.⁷ The parameter $Q = (n\Delta t)^{-1}$ is the annual tidal quality factor (where Δt is the constant tidal time lag), and it parameterizes the efficiency of tidal damping. These parameters are frequently combined into the “reduced tidal quality factor,” $Q' = 3Q/2k_2$.

Finally, we have also assumed in Equation (1) that the planet’s spin rotation frequency, $\omega = 2\pi/P_{\text{rot}}$, has reached an equilibrium (at which $d\omega/dt = 0$). This rate is given by

⁶ Note that this angle is distinct from the “stellar obliquity” most often referenced in the exoplanetary literature, which is the angle between the stellar spin axis and the planet’s orbital axis.

⁷ For reference, the estimates for Saturn, Uranus, and Neptune are $k_2 = 0.39$, 0.104, and 0.127, respectively (Gavrilov & Zharkov 1977; Lainey 2016).

(Leconte et al. 2010)

$$\omega_{\text{eq}} = n \frac{N(e)}{\Omega(e)} \frac{2 \cos \epsilon}{1 + \cos^2 \epsilon}. \quad (6)$$

The equilibrium rate reduces to synchronous rotation when $e = 0$ and $\epsilon = 0^\circ$.

In order to illustrate typical values of L_{tide} for sub-Saturns, we plot Equation (1) as a heatmap in Figure 1. The value of L_{tide} can reach up to $\sim 10^{29}$ erg s⁻¹, or roughly 1% of the incident stellar power, L_{irr} .

2.2. Planetary Thermal Evolution Modeling

We now consider how this tidal luminosity affects the structural properties of sub-Saturns. To do so, we employ the model developed by M19 for thermally evolving planetary envelopes while including tidal heating. Details of the model may be found in Section 3 of M19. In short, we assume a spherically symmetric, two-layer planet model consisting of a heavy element core and an H/He envelope with solar metallicity and helium fraction. The atmospheric envelope is evolved using the Modules for Experiments in Stellar Astrophysics (MESA; Paxton et al. 2011, 2013, 2015, 2018, and references therein) 1D stellar evolution code, including a range of modifications developed by Chen & Rogers (2016) that make the model specific to planets as opposed to stars.

The tidal heating is accounted for as an extra source of core luminosity, which amounts to depositing the tidal energy at the base of the atmospheric envelope. This approach was justified in M19 on the basis that solid cores likely have significantly lower tidal quality factors than the planetary envelopes they host (Storch & Lai 2014, 2015), although M19 also showed that the results are nearly identical as long as the heat is deposited at or below the atmosphere’s radiative-convective boundary. Qualitatively, this picture is similar to the hot Jupiter radius inflation problem (e.g., Bodenheimer et al. 2003; Batygin et al. 2011; Spiegel & Burrows 2013; Komacek & Youdin 2017). We note, however, that we do not account for ohmic dissipation or any other additional heating sources that are relevant for planets with $T_{\text{eq}} \gtrsim 1000$ K. This will lead to underestimated radius inflation for the few strongly irradiated planets that we will study in Section 4; neglecting this effect does not undermine our primary conclusions, but rather strengthens them.

In order to determine the magnitude of tidally induced radius inflation over a wide range of parameter space, M19 developed a suite of ~ 5000 planetary models varying in four principal parameters: the planet mass, M_p ; the fraction of mass in the H/He envelope, f_{env} ; the strength of the incident stellar radiation flux with respect to Earth’s, F/F_\oplus ; and the strength of the tidal dissipation, which was parameterized as

$$\Gamma \equiv \log_{10} \left[\frac{Q'(1 + \cos^2 \epsilon)}{\sin^2 \epsilon} \right] \quad (7)$$

via Equation (1) with $e = 0$. We note that $\log_{10} L_{\text{tide}}$ or $\log_{10}(L_{\text{tide}}/L_{\text{irr}})$ would be a more natural parameter choice than Γ . Using Γ maintains consistency with M19, where the goal was to isolate obliquity tides. We will soon show that the treatment is formally equivalent.

The host star was assumed to have solar properties, such that $F/F_\oplus = (a/\text{au})^{-2}$. The four principal parameters were randomly selected from log-uniform distributions across a wide

Table 1

Parameters and Their Ranges Used for the Set of Planet Models

| Parameter | Range |
|----------------------------|--------------|
| M_p/M_\oplus | (1, 70) |
| $\log_{10} f_{\text{env}}$ | (-2.5, -0.3) |
| $\log_{10} F/F_\oplus$ | (0, 3) |
| Γ | (3, 7) |

range of parameter space. For each set of parameters, two models were generated and evolved for 10 Gyr: one model including tidal heating and one without. The planet radii in each case were directly compared.

The simulations in M19 were confined to $M_p < 20 M_\oplus$ and $f_{\text{env}} < 30\%$. Here, we must extend the parameter space. We generated $\sim 10,000$ new models, with the ranges of the four principal parameters listed in Table 1. We note that, while Γ is still parameterized using the $e = 0$ case, we will later use a transformation of this parameter to generalize the simulations to $e \neq 0$.

2.3. MCMC Parameter Estimation

With this expanded set of models in hand, the goal is to make inferences about the structures of observed planets after accounting for radius inflation due to tidal heating. To do this, we use the Markov Chain Monte Carlo (MCMC) fitting approach described in detail in Section 5.1 of M19. A demonstration of the procedure is provided at <https://github.com/smiholland/Sub-Saturns/>.

In brief, we first use the MESA simulation set to construct linear barycentric interpolation functions for R_p at 1, 2, ..., 10 Gyr in both the tides and tides-free models. The independent variables are the four principal parameters— M_p , f_{env} , F_p , and Γ —in the case with tides, and just the first three of these in the tides-free case. We then use the 5 Gyr⁸ interpolation functions as the radius models and employ the affine-invariant ensemble sampler emcee (Goodman & Weare 2010; Foreman-Mackey et al. 2013) to estimate the posterior distributions of the parameters consistent with the planets’ observed radii. We use uniform priors and a Gaussian likelihood function, and we collect 10,000 samples across 200 chains, discarding the first 5000 samples as burn-in. Convergence is assessed by inspecting the trace plots to see that the chains are well-mixed. We also calculate the Gelman-Rubin statistic (Gelman & Rubin 1992) for each parameter and ensure that it is stable and close to unity.

Within the MCMC, we fix F/F_\oplus to the observed value, and let M_p float within 3σ uncertainties. As a result, the only essential free parameter in the tides-free model is f_{env} . In the model that includes tides, Γ is a second free parameter. We will use the notation $f_{\text{env},0}$ and $f_{\text{env},t}$ to refer to the envelope mass fractions obtained from parameter inferences in the case without tides and with tides, respectively.

The output products of this MCMC procedure are the posterior distributions. In the case of the fit that includes tides, we must apply one final transformation to make the results generalizable. This is because the MESA simulations, as noted in Section 2.2, assumed $e = 0$ and solar parameters. To allow

the posterior distribution to correspond to arbitrary e and stellar parameters, we must transform Q' in a way that forces L_{tide} to be invariant. To illustrate this, we let the subscript “ i ” correspond to the initial results using $e = 0$ and solar parameters. Explicitly, we note that $M_{*i} = M_\odot$ and $a_i/\text{au} = (F/F_\oplus)^{-1/2}$. The parameters without subscripts will correspond to the actual system, with arbitrary e , a , ϵ , and stellar parameters. Using Equations (1) and (7) and setting $L_{\text{tide}}(e, \epsilon) = L_{\text{tide},i}(e_i = 0, \epsilon_i)$, we obtain

$$Q' = Q'_i \frac{(1 + \cos^2 \epsilon_i)}{\sin^2 \epsilon_i} \left(\frac{M_*}{M_{*i}} \right)^2 \left(\frac{n}{n_i} \right) \left(\frac{a_i}{a} \right)^6 \times \left[N_a(e) - \frac{N^2(e)}{\Omega(e)} \frac{2 \cos^2 \epsilon}{1 + \cos^2 \epsilon} \right]. \quad (8)$$

This transformation allows us to take the original posterior distribution in $\Gamma_i = \log_{10}[Q'_i(1 + \cos^2 \epsilon_i)/\sin^2 \epsilon_i]$ and, for a given e , ϵ , M_* , and a (the latter two of which give us n), transform it into a posterior distribution in $\log_{10} Q'$. By working in log space, the Jacobian of the transformation is unity.

In Sections 3 and 4, we will employ this MCMC fitting procedure to estimate the parameters of planets whose structures may have been significantly altered by tidal inflation.

3. Case Study of the K2-19 System

We begin with a case study of the K2-19 system, since the recent analysis of this system by Petigura et al. (2020) was the motivation for this work, and the planetary masses and radii have been constrained at the $\sim 5\%$ level. The system contains three known transiting planets: two sub-Saturns K2-19 b and c, with orbital periods of 7.9 days and 11.9 days, respectively, as well as K2-19 d, a close-in Earth-size planet at 2.5 days. The outer two planets are interacting in an eccentric ($e \sim 0.2$) 3:2 mean-motion resonance.⁹ See Table 2 for a list of the relevant parameters.

Using interpolation to the Lopez & Fortney (2014) core-envelope planet model grid (which does not include tidal heating), Petigura et al. (2020) estimated that planets b and c have large envelope mass fractions, $f_{\text{env},b} = 44\% \pm 3\%$ and $f_{\text{env},c} = 14\% \pm 1\%$. As discussed in the introduction, planet b’s near-50% inferred envelope fraction presents a particular challenge to core accretion theory. Here, we investigate revisions to these estimates when we account for tidal heating.

3.1. Inferences of f_{env} when Including Tides

Figure 2 shows the envelope fraction estimates resulting from our MCMC analysis. The top and bottom panels show the results for K2-19 b and K2-19 c, respectively. The mean and 1σ range of $f_{\text{env},0}$ inferred when neglecting tides are shown with the gray line and bar. The tides-free envelope fraction estimates are $f_{\text{env},0} = 44.2\% \pm 2.8\%$ for K2-19 b and $f_{\text{env},0} = 14.2\% \pm 2.0\%$ for K2-19 c, which are both consistent with the estimates from Petigura et al. (2020). The agreement is reassuring, given that these estimates were obtained with two distinct core-envelope models.

⁸ The choice of 5 Gyr is arbitrary; any age past 1 Gyr works equally well. The radii asymptote to equilibrium values by ~ 1 Gyr as the planets radiate away their heat of formation.

⁹ While Petigura et al. (2020) found that the standard resonant angles all circulated rather than librated, Petit et al. (2020) find that a set of angles emerging from the Sessin–Henrard transformation (Batygin & Morbidelli 2013) do in fact librate.

Table 2
 Parameters of the K2-19 System from Petigura et al. (2020)

| Parameter | Value |
|--------------------------|----------------------|
| Star | |
| M_* (M_\odot) | 0.88 ± 0.03 |
| R_* (R_\odot) | 0.82 ± 0.03 |
| T_{eff} (K) | 5322 ± 100 |
| Planet b | |
| P_b (days) | 7.9222 ± 0.0001 |
| e_b | 0.20 ± 0.03 |
| i_b (deg) | 91.5 ± 0.1 |
| F_b (F_\oplus) | 87.0 ± 9.5 |
| $M_{p,b}$ (M_\oplus) | 32.4 ± 1.7 |
| $R_{p,b}$ (R_\oplus) | 7.0 ± 0.2 |
| Planet c | |
| P_c (days) | 11.8993 ± 0.0008 |
| e_c | 0.21 ± 0.03 |
| i_c (deg) | 91.1 ± 0.1 |
| F_c (F_\oplus) | 50.6 ± 5.6 |
| $M_{p,c}$ (M_\oplus) | 10.8 ± 0.6 |
| $R_{p,c}$ (R_\oplus) | 4.1 ± 0.2 |
| Planet d | |
| P_d (days) | 2.5081 ± 0.0002 |
| e_d | 0 (fixed) |
| i_d (deg) | 90.8 ± 0.7 |
| F_d (F_\oplus) | 403.2 ± 44.5 |
| $M_{p,d}$ (M_\oplus) | < 10 |
| $R_{p,d}$ (R_\oplus) | 1.11 ± 0.05 |

The colored regions in Figure 2 indicate the 2D posterior distributions in $\log_{10} Q'$ and $f_{\text{env},t}$ from the fit that includes tidal inflation. These distributions assume the measured eccentricities and indicate the results for three values of the obliquity ($\epsilon = 0^\circ, 30^\circ, 60^\circ$). There is a strong covariance between $\log_{10} Q'$ and $f_{\text{env},t}$: lower values of Q' result in stronger tidal heating, greater amounts of radius inflation, and smaller envelope fraction estimates.

For planets in this class size, the most reasonable estimate of Q' is in the range $\sim 10^4$ – 10^5 , based on analogy with Saturn (Murray & Dermott 1999), Uranus (Tittlemore & Wisdom 1989), and Neptune (Zhang & Hamilton 2008), as well as the few sub-Neptune and Neptune-mass exoplanets with Q' constraints. These include the Neptune-mass GJ 436 b ($Q' \sim 10^5$; Morley et al. 2017) and the sub-Neptune-mass GJ 876 d ($Q' \sim 10^4$ – 10^5 ; Puranam & Batygin 2018). However, we can obtain another rough constraint on Q' by considering that the timescale for the orbit to circularize must be greater than the system age, since the planets are observed with nonzero eccentricities today. The tidal circularization timescale is given by (Leconte et al. 2010)

$$\tau_e = \frac{e}{\dot{e}} = \frac{4}{99} \left(\frac{Q'}{n} \right) \left(\frac{M_p}{M_*} \right) \left(\frac{a}{R_p} \right)^5 \times \left[\Omega_e(e) \cos \epsilon \left(\frac{\omega}{n} \right) - \frac{18}{11} N_e(e) \right]^{-1}, \quad (9)$$

where we have introduced additional functions of eccentricity (to add to those from Equations (2)–(4)),

$$\Omega_e(e) = \frac{1 + \frac{3}{2}e^2 + \frac{1}{8}e^4}{(1 - e^2)^5} \quad (10)$$

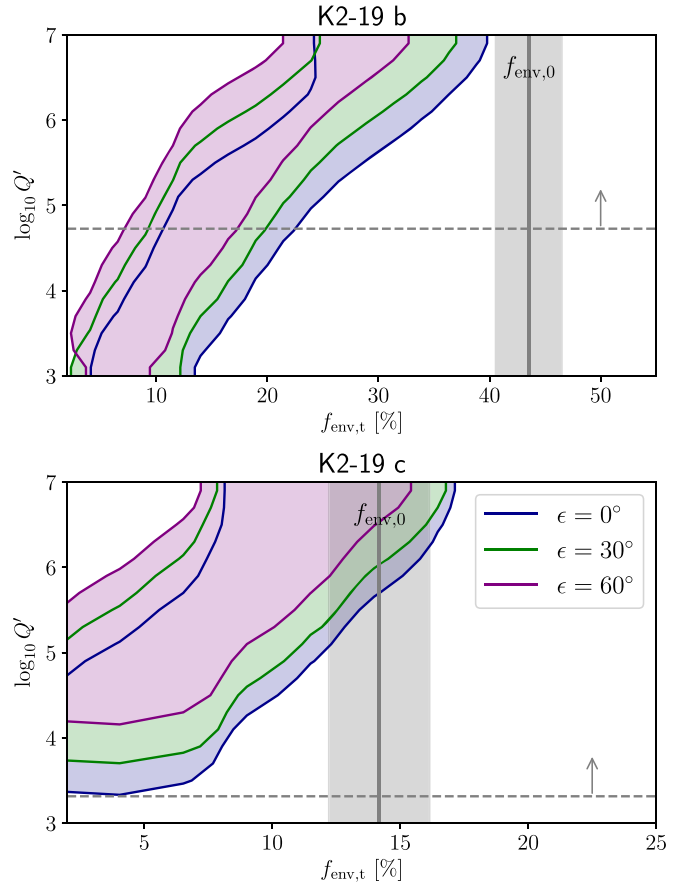


Figure 2. Comparison of the envelope mass fraction estimates with tides ($f_{\text{env},t}$) and without tides ($f_{\text{env},0}$) of K2-19 b (top panel) and K2-19 c (bottom panel). Vertical gray bars correspond to the mean and standard deviation of $f_{\text{env},0}$. These values are $f_{\text{env},0} = 44.2\% \pm 2.8\%$ for K2-19 b and $f_{\text{env},0} = 14.2\% \pm 2.0\%$ for K2-19 c. Colored regions indicate the 2σ contours of the posterior distributions of $\log_{10} Q'$ and $f_{\text{env},t}$ after accounting for tides. These assume the eccentricities from Table 2, and the separate colors indicate different obliquities ($\epsilon = 0^\circ, 30^\circ, 60^\circ$). Horizontal dashed lines indicate the lower limit $\log_{10} Q'_{\text{low}}$ such that $\tau_e > 1$ Gyr.

$$N_e(e) = \frac{1 + \frac{15}{4}e^2 + \frac{15}{8}e^4 + \frac{5}{64}e^6}{(1 - e^2)^{\frac{13}{2}}}. \quad (11)$$

While the stellar age is poorly constrained, we can place an approximate lower limit by assuming $\tau_{\text{age}} \gtrsim 1$ Gyr.¹⁰ Accordingly, we can calculate the lower limit of Q' , which we shall denote as Q'_{low} , such that $\tau_e > 1$ Gyr. In calculating this, we will assume that $\epsilon = 0^\circ$ and that $\omega = \omega_{\text{eq}}$. The resulting limits are $Q'_{\text{low}} > 5.3 \times 10^4$ for K2-19 b and $Q'_{\text{low}} > 2.1 \times 10^3$ for K2-19 c. These are indicated with horizontal dashed lines in Figure 2. We note that the Q'_{low} estimates are generally conservative, since the system could be younger than 1 Gyr and the planets could have started with significantly larger eccentricities.

We note that there is yet another available constraint on Q' by considering the angular momentum deficit reservoir. That is, the orbital decay induced by tidal dissipation must be balanced by sufficient damping of the eccentricities and mutual orbital inclinations, such that the system's total angular momentum is conserved. This constraint, however, is generally less stringent

¹⁰ Consulting gyrochronology relationships, the 20 day rotation period implies an age of > 1 Gyr (T. David 2020, private communication).

than the limit imposed by the tidal circularization timescale, since it involves both eccentricity and inclination damping, as opposed to eccentricity damping alone.

Considering the lower limits on Q' , we see that K2-19 b's $f_{\text{env},t}$ could be as small as $\sim 5\%$ – 20% , depending on the obliquity. Even with large values of $\log_{10} Q'$, however, we see that the estimate of $f_{\text{env},t}$ is well below $f_{\text{env},0}$, thus resolving the tension produced by the original, tides-free estimate being so near 50%. For K2-19 c, the impact of tidal heating is less extreme than it is for planet b, but K2-19 c's $f_{\text{env},t}$ is also well below the tides-free estimate. We also observe that it is possible that the planets have similar intrinsic envelope fractions. For instance, if both planets have $Q' \sim 10^5$, and if $\epsilon_b \sim 60^\circ$ and $\epsilon_c \sim 0^\circ$, then they would both have $f_{\text{env},t} \sim 7\%$ – 12% . With values this small, planets b and c would both be considered to be sub-Neptunes if they were not tidally inflated. That is, with $f_{\text{env}} = 7\%$ and no tidal heating, the planets would have radii equal to $R_{p,b} \sim 3.9 R_\oplus$ and $R_{p,c} \sim 3.3 R_\oplus$. These sizes are at the upper end of the sub-Neptune range (1.8–4.0 R_\oplus ; Petigura et al. 2018b), suggesting that the K2-19 planets can be interpreted as sub-Neptunes that underwent significant tidal heating.

Finally, we note that Figure 2 indicates that eccentricity tides alone are sufficient to induce appreciable modifications to the f_{env} estimates, but obliquity tides may be just as impactful. It is therefore worth investigating the possibility of obliquity enhancement for the K2-19 planets. We address this in the Appendix. To summarize, we find that K2-19 b is particularly susceptible to secular spin–orbit resonances that excite the planet's obliquity to large values ($\epsilon \sim 60^\circ$). While it is difficult to determine whether this obliquity excitation has in fact transpired, it is clear that obliquity tides may be playing an important role in K2-19 b.

4. Sub-Saturn Population Analysis

The case study of the K2-19 system has confirmed that tidally induced radius inflation can resolve the near-50% envelope fraction estimate of K2-19 b, taking it as low as $\sim 5\%$ – 20% . It can also reduce K2-19 c's estimate by $\gtrsim 10\%$. This example raises questions about the degree to which other sub-Saturns have been shaped by tidal inflation. In this section, we apply the methodology developed in Section 3 to the sub-Saturn population as a whole.

We begin by defining the planet sample. We use the NASA Exoplanet Archive (NEA; Akesson et al. 2013) to extract all planets with radii in the range 4.0–8.0 R_\oplus that also have measured masses. We remove circumbinary planets and planets with unreliable measurements, such as those with masses based on 10 RVs or less. Where available, we update the planetary and stellar parameters with more precise constraints. We use the parameter tables from Fulton & Petigura (2018), who combined parallaxes from Gaia Data Release 2 (DR2; Gaia Collaboration et al. 2018) and spectroscopy from the California-Kepler Survey (CKS; Petigura et al. 2017a; Johnson et al. 2017) to update parameters for the Kepler planets and planet candidates.

For the K2 planets, we use tables from Hardegree-Ullman et al. (2020), who similarly derived updated parameters using Gaia DR2 and spectroscopy from the Large Sky Area Multi-Object Fibre Spectroscopic Telescope (LAMOST) DR5 (Cui et al. 2012). We only update the stellar and planetary parameters (specifically R_p , R_* , a , T_{eff} , and F/F_\oplus) when the

precision of the R_p measurement is less than the literature value from NEA (which is true for most cases). Finally, for the Kepler planets with M_p measured by Transit Timing Variations, we use the parameter estimates from the uniform analysis performed by Hadden & Lithwick (2017) if they are more precise than the NEA masses.

Using the updated masses and radii, we calculate bulk densities and extract the planets with densities measured to 50% or better. Due to the constraints imposed by the MESA simulations (Section 2.2), we can only study planets with $M_p < 70 M_\oplus$ and $F/F_\oplus \in (0, 10^3)$. Three planets were removed due to these constraints. The final sample is similar to that assembled by Petigura et al. (2017b), supplemented by ~ 15 additional planets that have been discovered since their analysis. Within this list, we include TOI-257 b (Addison et al. 2020) and TOI-421 b (Carleo et al. 2020), two recently discovered sub-Saturns that had not yet been incorporated into the NEA.

For each sub-Saturn in the sample, we apply the MCMC analysis that was described in Section 2.3 and utilized for the K2-19 planets in Section 3.1. We assume fixed eccentricities at the measured values, thus ignoring the effects of any perturbing bodies (observed or unobserved) that might be driving secular eccentricity oscillations and time-variable radius inflation. Such oscillations will only affect our inferences at a detailed level. For cases where e was fixed to zero, we assumed a fiducial value equal to $e = 0.05$. We obtain envelope fraction estimates of the planets according to the two models with and without tidal inflation. The estimates of $f_{\text{env},0}$ are calculated using the mean and standard deviation of the posterior distributions from the tides-free fit. The estimates of $f_{\text{env},t}$ are calculated by first marginalizing the 2D posterior distributions of $f_{\text{env},t}$ and $\log_{10} Q'$ (e.g., see Figure 2) by summing them over a range in $\log_{10} Q'$. If $\log_{10} Q'_{\text{low}} < 4$, we use the range $\log_{10} Q' \in [4, 5]$. Otherwise, we use the range $\log_{10} Q' \in [\log_{10} Q'_{\text{low}}, \log_{10} Q'_{\text{low}} + 1]$. Finally, we calculate the mean and standard deviation of this marginalized posterior distribution.

The results of this population analysis are summarized in Figure 3 and Table 3. For each planet, we show the $f_{\text{env},0}$ and $f_{\text{env},t}$ estimates connected by a line. The two estimates are plotted against L_{tide} in order to examine how the difference in estimates depends on the tidal strength. We observe that most planets have adjustments to their envelope fraction estimates of at least $f_{\text{env},0} - f_{\text{env},t} \sim 5\%$; the average value is $\langle f_{\text{env},0} - f_{\text{env},t} \rangle = 10\%$. In the bottom panel of Figure 3, we show histograms of $f_{\text{env},0}$ and $f_{\text{env},t}$. Without accounting for tidal inflation, roughly 70% of planets are inferred to have $f_{\text{env},0} > 15\%$. In contrast, after accounting for tidal inflation, only 35% of planets have $f_{\text{env},t} > 15\%$.

The cases of greatest interest are those with $f_{\text{env},0} \sim 50\%$. Seven planets have $f_{\text{env},0} > 40\%$. These are (from smallest to largest radius) K2-19 b, TOI-257 b, HAT-P-26 b, WASP-166 b, Kepler-79 d, HD 89345 b, and K2-24 c. We plot these cases in Figure 4. For convenience of comparison, we include K2-19 b, although it was studied in detail in Section 3.

All cases except Kepler-79 d and K2-24 c are unequivocally resolved by including tidal heating, since they have $f_{\text{env},t} \sim 10\%$, even with $\epsilon = 0^\circ$. As for Kepler-79 d and K2-24 c, the fit results indicate that both planets would have $f_{\text{env},t} \sim 40\%$ – 50% if $\epsilon = 0^\circ$. To get $f_{\text{env},t} < 30\%$ with tidal inflation would require $\epsilon \gtrsim 30^\circ$. Alternatively, there may be

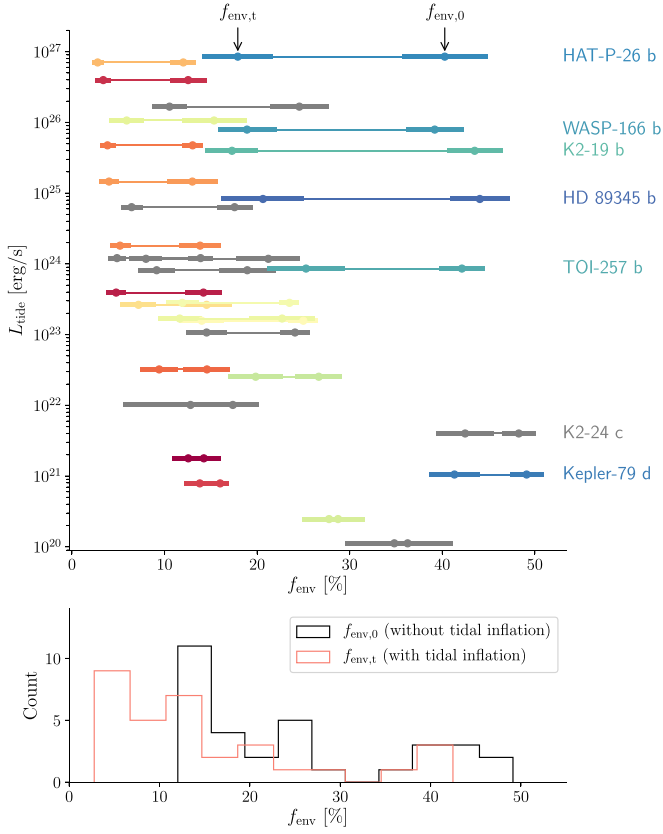


Figure 3. Comparison of the envelope mass fraction estimates with tides ($f_{\text{env},t}$) and without tides ($f_{\text{env},0}$) across the sub-Saturn population. Top panel: on the x-axis, we show the two estimates for each planet, where the dot and thick part of the line indicate the posterior mean and standard deviation, respectively. An example is labeled with arrows. The two estimates are connected horizontally in order to indicate the magnitude of the drop in envelope fraction. Color corresponds to R_p (redder = smaller, bluer = larger), and gray lines are the cases with poor eccentricity constraints. The y-axis shows the value of L_{tide} , calculated assuming fiducial values of $Q' = 10^5$ and $\epsilon = 30^\circ$. We observe that the change in f_{env} between the models with and without tides becomes more significant for larger L_{tide} . Bottom panel: histograms of the posterior mean point estimates. Black summarizes the results without tidal inflation, and red summarizes the results with tidal inflation.

other explanations for these planets’ anomalously large radii, e.g., that they are young planets undergoing dusty hydrodynamic outflows (Wang & Dai 2019) and/or that they contain high-altitude photochemical hazes that are enhancing their observed radii (Gao & Zhang 2020; Libby-Roberts et al. 2020).

5. Discussion

5.1. Sub-Saturns as Inflated Sub-Neptunes

We have shown that many sub-Saturns have likely undergone significant radius inflation due to tidal heating. The fact that these planets’ radii are influenced by their dynamical state (specifically eccentricity and obliquity)—and not just their physical properties—motivates questions surrounding their contextualization within the broader short-period planet population. In other words, many sub-Saturns with $4.0\text{--}8.0 R_{\oplus}$ may only exist in this radius range because they have been inflated, and their intrinsic envelope fractions may be more consistent with sub-Neptunes, with radii in the range $1.8\text{--}4.0 R_{\oplus}$.

To investigate this, we plot in Figure 5 the comparison between the observed radii of the planets in the sample and the

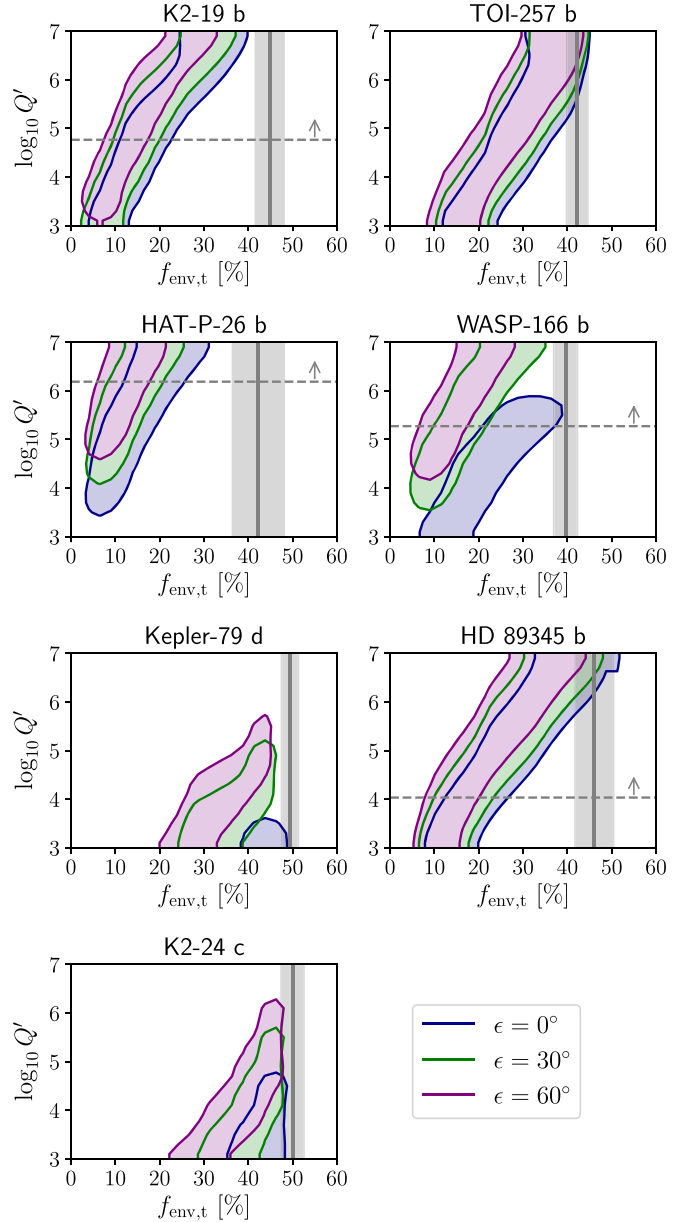


Figure 4. Analysis of all planets with $f_{\text{env},0} > 40\%$ before accounting for tidal inflation, including K2-19 b, which was also shown in Figure 2. As in Figure 2, we show comparisons of the envelope fraction estimates with tides ($f_{\text{env},t}$) and without tides ($f_{\text{env},0}$). Vertical gray bars correspond to the mean and standard deviation of $f_{\text{env},0}$. Colored regions indicate the 2σ contours of the posterior distributions of $\log_{10} Q'$ and $f_{\text{env},t}$ after accounting for tides. These assume the measured eccentricities from Table 3, and the separate colors indicate different obliquities. Horizontal dashed lines indicate the lower limit $\log_{10} Q'_{\text{low}}$ such that $\tau_e > 1$ Gyr. These lines are not pictured for the three cases (TOI-257 b, Kepler-79 d, K2-24 c) where it is below $\log_{10} Q' = 3$.

radii the planets would have if they were not tidally inflated. This estimate is calculated assuming intrinsic envelope fractions equal to $f_{\text{env},t}$ (from Table 3) and using the radius interpolation functions discussed in Section 2.3. The observed radii are larger than the tides-free radii by a factor of 1.3 on average. Nearly half of the planets would be considered sub-Neptunes if they were not experiencing tidal inflation. In this sense, these planets can be interpreted as the tail end of the sub-Neptune group, which have $f_{\text{env}} \lesssim 10\%$.

Table 3
Population Analysis of Sub-Saturns with Densities Measured to 50% or Better

| Name | P (days) | R_p (R_\oplus) | M_p (M_\oplus) | ρ (g cm^{-3}) | e | $f_{\text{env},0}$ (%) | $f_{\text{env},t}$ (%) | $\log_{10} Q'_{\text{low}}$ | |
|------|---------------|----------------------|------------------------|-------------------------------|------------------------|------------------------------|------------------------|-----------------------------|-----|
| 1 | Kepler-82 b | 26.44 | $4.07^{+0.24}_{-0.1}$ | $12.2^{+1.0}_{-0.9}$ | $0.99^{+0.11}_{-0.19}$ | $0.0033^{+0.0019}_{-0.0002}$ | 14.2 ± 1.8 | 12.6 ± 1.7 | 1.6 |
| 2 | K2-19 c | 11.899 | $4.1^{+0.2}_{-0.2}$ | $10.8^{+0.6}_{-0.6}$ | $0.86^{+0.14}_{-0.14}$ | $0.21^{+0.03}_{-0.03}$ | 14.2 ± 2.0 | 4.8 ± 1.0 | 3.3 |
| 3 | GJ 436 b | 2.644 | $4.17^{+0.17}_{-0.17}$ | $22.1^{+2.3}_{-2.3}$ | $1.68^{+0.27}_{-0.27}$ | $0.1383^{+0.0002}_{-0.0002}$ | 12.6 ± 2.0 | 3.4 ± 0.8 | 6.0 |
| 4 | Kepler-11 e | 32.0 | $4.19^{+0.07}_{-0.09}$ | $6.7^{+1.2}_{-1.0}$ | $0.5^{+0.1}_{-0.08}$ | $0.012^{+0.006}_{-0.006}$ | 16.0 ± 0.9 | 13.8 ± 1.7 | 1.5 |
| 5 | Kepler-18 c | 7.642 | $4.27^{+0.11}_{-0.11}$ | $17.3^{+1.9}_{-1.9}$ | $1.23^{+0.16}_{-0.16}$ | ... | 13.9 ± 1.3 | 4.9 ± 1.0 | 3.9 |
| 6 | HD 106315 c | 21.057 | $4.35^{+0.23}_{-0.23}$ | $15.2^{+3.7}_{-3.7}$ | $1.02^{+0.3}_{-0.3}$ | $0.22^{+0.15}_{-0.15}$ | 14.6 ± 2.5 | 9.4 ± 2.0 | 2.2 |
| 7 | HAT-P-11 b | 4.888 | $4.36^{+0.06}_{-0.06}$ | $26.7^{+2.2}_{-2.2}$ | $1.77^{+0.17}_{-0.17}$ | $0.218^{+0.034}_{-0.031}$ | 13.0 ± 1.1 | 3.8 ± 0.8 | 4.8 |
| 8 | Kepler-411 c | 7.834 | $4.42^{+0.06}_{-0.06}$ | $26.4^{+5.9}_{-5.9}$ | $1.68^{+0.38}_{-0.38}$ | $0.108^{+0.003}_{-0.004}$ | 13.8 ± 2.2 | 5.2 ± 1.1 | 3.8 |
| 9 | K2-27 b | 6.771 | $4.48^{+0.23}_{-0.23}$ | $30.9^{+4.6}_{-4.6}$ | $1.89^{+0.41}_{-0.41}$ | $0.251^{+0.088}_{-0.088}$ | 13.0 ± 2.7 | 4 ± 1.1 | 4.2 |
| 10 | Kepler-33 d | 21.776 | $4.53^{+0.14}_{-0.14}$ | $3.9^{+1.9}_{-1.8}$ | $0.23^{+0.11}_{-0.11}$ | ... | 17.4 ± 2.6 | 12.8 ± 7.3 | 2.6 |
| 11 | Kepler-1656 b | 31.579 | $4.57^{+0.11}_{-0.11}$ | $48.6^{+4.2}_{-3.8}$ | $2.8^{+0.31}_{-0.29}$ | $0.836^{+0.013}_{-0.012}$ | 12.0 ± 1.4 | 2.8 ± 0.6 | 4.7 |
| 12 | HD 219666 b | 6.036 | $4.71^{+0.17}_{-0.17}$ | $16.6^{+1.3}_{-1.3}$ | $0.88^{+0.12}_{-0.12}$ | ... | 17.6 ± 1.9 | 6.4 ± 1.2 | 4.5 |
| 13 | Kepler-56 b | 10.502 | $4.77^{+0.21}_{-0.21}$ | $22.1^{+3.9}_{-3.6}$ | $1.12^{+0.25}_{-0.24}$ | $0.04^{+0.01}_{-0.01}$ | 14.5 ± 2.7 | 7.2 ± 1.9 | 3.1 |
| 14 | K2-32 b | 8.992 | $4.96^{+0.33}_{-0.27}$ | $16.5^{+2.7}_{-2.7}$ | $0.75^{+0.17}_{-0.19}$ | ... | 21.2 ± 3.4 | 8 ± 1.8 | 3.9 |
| 15 | Kepler-18 d | 14.859 | $5.11^{+0.13}_{-0.13}$ | $16.4^{+1.4}_{-1.4}$ | $0.68^{+0.08}_{-0.08}$ | ... | 24.1 ± 1.6 | 14.5 ± 2.2 | 3.0 |
| 16 | TOI-421 b | 16.068 | $5.17^{+0.13}_{-0.13}$ | $16.2^{+1.1}_{-1.1}$ | $0.62^{+0.07}_{-0.07}$ | $0.152^{+0.042}_{-0.045}$ | 25.0 ± 1.6 | 14 ± 2.4 | 3.0 |
| 17 | K2-98 b | 10.136 | $5.2^{+0.19}_{-0.19}$ | $32.2^{+8.1}_{-8.1}$ | $1.26^{+0.35}_{-0.35}$ | ... | 18.9 ± 3.0 | 9.1 ± 2.0 | 3.4 |
| 18 | Kepler-25 c | 12.721 | $5.22^{+0.07}_{-0.06}$ | $15.2^{+1.3}_{-1.6}$ | $0.59^{+0.06}_{-0.07}$ | $0.0061^{+0.0049}_{-0.0041}$ | 23.5 ± 1.1 | 11.9 ± 1.7 | 3.4 |
| 19 | Kepler-223 d | 14.789 | $5.24^{+0.26}_{-0.45}$ | $8.0^{+1.5}_{-1.3}$ | $0.31^{+0.1}_{-0.07}$ | $0.037^{+0.018}_{-0.017}$ | 22.7 ± 3.6 | 11.6 ± 2.3 | 3.5 |
| 20 | K2-108 b | 4.734 | $5.33^{+0.21}_{-0.21}$ | $59.4^{+4.4}_{-4.4}$ | $2.16^{+0.3}_{-0.3}$ | $0.18^{+0.042}_{-0.042}$ | 15.3 ± 3.5 | 5.9 ± 1.9 | 4.8 |
| 21 | Kepler-82 c | 51.54 | $5.34^{+0.32}_{-0.13}$ | $13.9^{+1.3}_{-1.2}$ | $0.5^{+0.06}_{-0.1}$ | $0.007^{+0.0016}_{-0.0018}$ | 28.7 ± 2.9 | 27.8 ± 2.9 | 0.9 |
| 22 | K2-24 b | 20.89 | $5.4^{+0.2}_{-0.2}$ | $19.0^{+2.2}_{-2.1}$ | $0.66^{+0.11}_{-0.1}$ | $0.06^{+0.01}_{-0.01}$ | 26.7 ± 2.5 | 19.8 ± 2.9 | 2.4 |
| 23 | WASP-156 b | 3.836 | $5.72^{+0.22}_{-0.22}$ | $40.7^{+3.2}_{-2.9}$ | $1.2^{+0.17}_{-0.16}$ | ... | 24.6 ± 3.2 | 10.5 ± 1.9 | 5.5 |
| 24 | Kepler-87 c | 191.232 | $6.14^{+0.29}_{-0.29}$ | $6.4^{+0.8}_{-0.8}$ | $0.15^{+0.03}_{-0.03}$ | $0.039^{+0.012}_{-0.012}$ | 38.8 ± 3.6 | 38.6 ± 3.5 | ... |
| 25 | Kepler-297 c | 74.92 | $6.35^{+0.19}_{-0.19}$ | $42.1^{+14.1}_{-9.3}$ | $0.9^{+0.31}_{-0.22}$ | ... | 36.3 ± 4.9 | 34.8 ± 5.2 | 0.1 |
| 26 | K2-19 b | 7.922 | $7.0^{+0.2}_{-0.2}$ | $32.4^{+1.7}_{-1.7}$ | $0.52^{+0.05}_{-0.05}$ | $0.2^{+0.03}_{-0.03}$ | 44.2 ± 2.8 | 17.3 ± 2.8 | 4.8 |
| 27 | TOI-257 b | 18.388 | $7.02^{+0.15}_{-0.13}$ | $42.6^{+7.3}_{-7.0}$ | $0.68^{+0.12}_{-0.12}$ | $0.242^{+0.04}_{-0.065}$ | 42.1 ± 2.5 | 25.3 ± 4.2 | 3.0 |
| 28 | WASP-166 b | 5.444 | $7.06^{+0.34}_{-0.34}$ | $32.1^{+1.6}_{-1.6}$ | $0.5^{+0.08}_{-0.08}$ | $0.03^{+0.02}_{-0.02}$ | 39.2 ± 3.1 | 18.9 ± 3.2 | 5.3 |
| 29 | HAT-P-26 b | 4.235 | $7.06^{+0.45}_{-0.45}$ | $22.2^{+6.4}_{-6.4}$ | $0.35^{+0.12}_{-0.12}$ | $0.12^{+0.06}_{-0.06}$ | 40.3 ± 4.6 | 17.9 ± 3.8 | 6.2 |
| 30 | Kepler-79 d | 52.09 | $7.16^{+0.13}_{-0.16}$ | $6.0^{+2.1}_{-1.6}$ | $0.09^{+0.03}_{-0.02}$ | $0.025^{+0.059}_{-0.023}$ | 49.1 ± 1.8 | 41.3 ± 2.7 | 1.8 |
| 31 | HD 89345 b | 11.814 | $7.4^{+0.31}_{-0.34}$ | $35.0^{+5.4}_{-5.7}$ | $0.48^{+0.1}_{-0.1}$ | $0.22^{+0.095}_{-0.13}$ | 44.1 ± 3.2 | 20.6 ± 4.5 | 4.0 |
| 32 | K2-24 c | 42.339 | $7.5^{+0.3}_{-0.3}$ | $15.4^{+1.9}_{-1.8}$ | $0.2^{+0.03}_{-0.03}$ | <0.07 | 48.3 ± 1.8 | 42.5 ± 3.1 | 1.9 |

Notes. Here, $f_{\text{env},0}$ is the envelope mass fraction estimate when tidal inflation is neglected, and $f_{\text{env},t}$ is the estimate including tidal inflation. The estimates of $f_{\text{env},t}$ assumed the measured eccentricities and fiducial 30° obliquities. In addition, $\log_{10} Q'_{\text{low}}$ is a conservative lower limit such that $\tau_e > 1$ Gyr. (See Section 3.1 for details.) Notes on individual systems: Kepler-82 b—Freudenthal et al. (2019), K2-19 c—Petigura et al. (2020), GJ 436 b—Maciejewski et al. (2014), Kepler-11 e—Lissauer et al. (2013), Kepler-18 c—Cochran et al. (2011), HD 106315 c—Barros et al. (2017), HAT-P-11 b—Yee et al. (2018), Kepler-411 c—Sun et al. (2019), K2-27 b—Petigura et al. (2017b), Kepler-33 d—Lissauer et al. (2012); Hadden & Lithwick (2017), Kepler-1656 b—Brady et al. (2018), HD 219666 b—Esposito et al. (2019), Kepler-56 b—Huber et al. (2013), K2-32 b—Heller et al. (2019), Kepler-18 d—Cochran et al. (2011), TOI-421 b—Carleo et al. (2020), K2-98 b—Livingston et al. (2018); Barragán et al. (2016), Kepler-25 c—Mills et al. (2019), Kepler-223 d—Mills et al. (2016), K2-108 b—Petigura et al. (2017b); Livingston et al. (2018) Kepler-82 c—Freudenthal et al. (2019), K2-24 b—Petigura et al. (2018a), WASP-156 b—Demangeon et al. (2018), Kepler-87 c—Ofir et al. (2014), Kepler-297 c—Rowe et al. (2014); Hadden & Lithwick (2014), K2-19 b—Petigura et al. (2020), TOI-257 b—Addison et al. (2020), WASP-166 b—Hellier et al. (2019), HAT-P-26 b—Hartman et al. (2011); Stassun et al. (2017), Kepler-79 d—Jontof-Hutter et al. (2014), HD 89345 b—Yu et al. (2018), K2-24 c—Petigura et al. (2018a).

5.2. Tidal Inflation Beyond $8.0 R_\oplus$

We emphasize that the $4.0 R_\oplus$ lower range of the sub-Saturn size class is arbitrary, chosen to be a round number near the size of Uranus/Neptune. Similarly, the $8.0 R_\oplus$ upper bound is an arbitrary classification. For RV surveys seeking to study sub-Jovian mass planets discovered by transit missions (e.g., Petigura et al. 2017b), $8.0 R_\oplus$ is a convenient threshold. Above this boundary, there is significant “contamination” of Jovian-mass planets. However, we should consider whether some planets above the $8.0 R_\oplus$ threshold may also be experiencing tidal inflation.

One such case is WASP-107 b, a low-density planet with a radius almost as large as Jupiter, $R_p = 10.5 \pm 0.2 R_\oplus$ (Anderson et al. 2017), but with a mass comparable to that of Neptune, $M_p = 30 \pm 2 M_\oplus$ (Piaulet et al. 2019). It orbits in $P = 5.7$ days

with $e = 0.13^{+0.03}_{-0.01}$ (Piaulet et al. 2019). This short-period orbit and nonzero eccentricity creates a substantial tidal luminosity, $L_{\text{tide}} \sim 10^{27}$ erg s^{-1} (with $Q' = 10^5$). In Figure 6, we show the results of our tidal inflation analysis for WASP-107 b, including 2D posteriors in $\log_{10} Q'$ and $f_{\text{env},t}$. The allowed regime indicated by the posteriors extends as low as $f_{\text{env},t} \sim 10\%$. While the constraint from the circularization timescale suggests that $Q' \gtrsim 10^6$, this case study indicates tidal inflation has likely had a significant impact for WASP-107 b and potentially other planets with $R_p > 8.0 R_\oplus$. We defer a uniform study of this population to future work.

5.3. Role of Atmospheric Mass Loss

There is ample evidence that early atmospheric mass loss, arising from photoevaporation driven by high-energy stellar

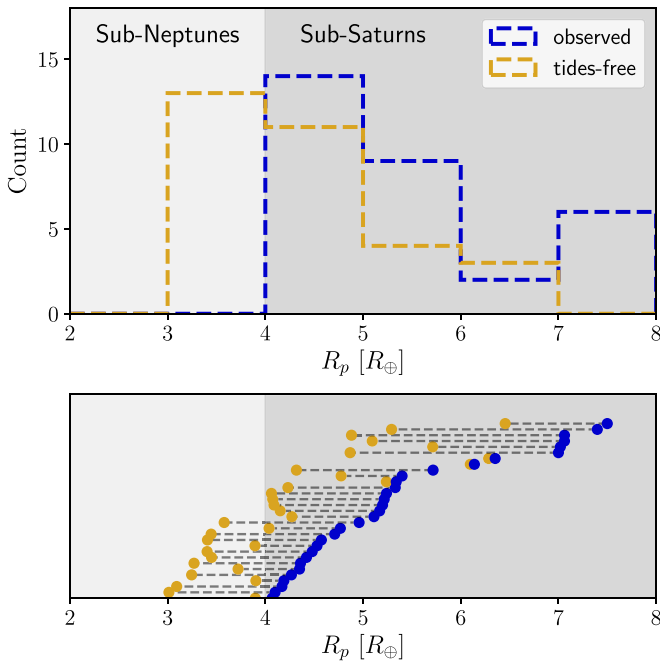


Figure 5. Comparison between the observed radii of the planets in the sample (blue) and the radii the planets would have if they were not tidally inflated (yellow), which were calculated assuming $f_{\text{env},t}$. We illustrate this with histograms (top panel) and with point estimates for each planet connected by lines and ordered by the observed radii (bottom panel). Nearly half of the planets in the sample would be considered sub-Neptunes ($1.8\text{--}4.0 R_{\oplus}$) if they were not tidally inflated into the sub-Saturn regime ($4.0\text{--}8.0 R_{\oplus}$).

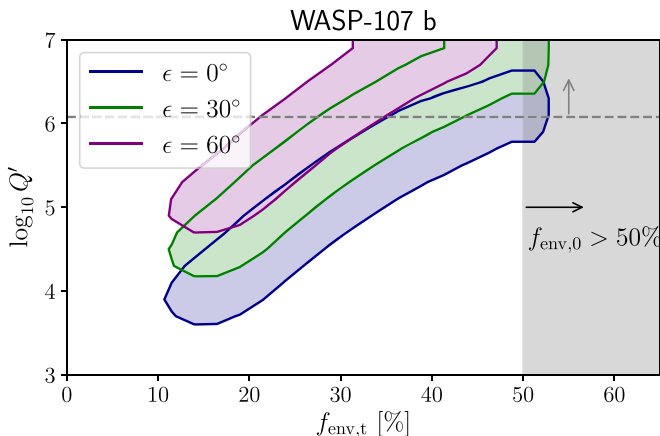


Figure 6. Analysis of WASP-107 b, an example of a planet with R_p larger than our $8.0 R_{\oplus}$ cutoff, but which nevertheless has likely been substantially affected by tidal inflation due to its high eccentricity ($e = 0.13$) and short orbital period ($P = 5.7$ days). Similar to Figures 2 and 4, the colored regions indicate the 2σ contours of the posterior distributions of $\log_{10} Q'$ and $f_{\text{env},t}$ after accounting for tides. These assume the measured eccentricity, and the separate colors indicate different obliquities. Envelope fraction estimate without tides is beyond $f_{\text{env},0} > 50\%$, which is the upper limit that our model can explore. Piaulet et al. (2019) estimated that it was $f_{\text{env},0} \sim 80\%$.

irradiation (e.g., Owen & Wu 2017) and/or heating from formation (e.g., Ginzburg et al. 2018), sculpts the short-period planetary radius distribution, creating a gap between super-Earths and sub-Neptunes (Fulton et al. 2017). This atmospheric erosion is also expected to impact short-period sub-Saturns, implying that their initial envelope mass fractions would have been even higher than today.

However, calculations of the instantaneous envelope mass-loss timescale, defined as $\tau_{\text{env}} = M_{\text{env}}/\dot{M}_p$, suggest that sub-Saturns probably did not lose much mass, due to their large cores and envelope fractions. For planets with $M_p \gtrsim 10 M_{\oplus}$ and $f_{\text{env}} \gtrsim 10\%$, Chen & Rogers (2016) found that the timescale for photoevaporative mass loss is $\tau_{\text{env}} \approx 10^9\text{--}10^{10}$ yr at early times when the stellar EUV is high. This long timescale is in contrast to that for low-mass planets with $M_p \lesssim 10 M_{\oplus}$ and $f_{\text{env}} \lesssim 1\%$, which can be as small as $\tau_{\text{env}} \sim 10^7$ yr. Consulting our MESA simulations from Section 2.2, we confirm that the sub-Saturns did not undergo significant photoevaporative mass loss; when $M_p > 10 M_{\oplus}$, $f_{\text{env}}(t=0) > 10\%$, and $F/F_{\oplus} > 50$, the loss in envelope fractions was almost always less than 1%.

5.4. Implications for Core Accretion

We have presented a resolution for the problematic planets with apparent $f_{\text{env}} \sim 50\%$, such that they are no longer situated at the brink of runaway accretion. However, in the process of better understanding their structures, this tidal framework has revealed some additional planets with unusual properties. Four planets in Table 3 have cores with $M_{\text{core}} > 30 M_{\oplus}$ after tidal inflation is accounted for: Kepler-1656 b with $M_{\text{core}} = 47.3 M_{\oplus}$ and $M_{\text{env}} = 1.3 M_{\oplus}$; K2-108 b with $M_{\text{core}} = 55.9 M_{\oplus}$ and $M_{\text{env}} = 3.5 M_{\oplus}$; WASP-156 b with $M_{\text{core}} = 36.4 M_{\oplus}$ and $M_{\text{env}} = 4.3 M_{\oplus}$; and TOI-257 b with $M_{\text{core}} = 31.8 M_{\oplus}$ and $M_{\text{env}} = 10.8 M_{\oplus}$. It is important to note that we would infer these planets to have large cores even when ignoring tides— $M_{\text{core}} = 42.8 M_{\oplus}$, $50.3 M_{\oplus}$, $30.7 M_{\oplus}$, and $24.7 M_{\oplus}$, respectively—but accounting for tides makes the envelope-to-core contrast even more extreme. These planets probably did not form via core accretion alone. A scattering and high-impact merger event could explain their massive cores, small envelopes, and enhanced eccentricities—particularly in the case of Kepler-1656 b, with $e = 0.836$, as discussed by Brady et al. (2018).

Planets with abnormally large cores aside, the majority of sub-Saturns have core masses greater than the $\sim 10 M_{\oplus}$ critical mass and yet are not gas giants. The problem of how and why they avoided runaway accretion is not unique to sub-Saturns. Many super-Earths and sub-Neptunes also have massive cores that could have reached runaway gas accretion before the dissipation of their disks (e.g., Lee et al. 2014). Various solutions to this have been proposed, including accretion in a high dust-to-gas ratio environment, which slows envelope cooling due to high opacities (Lee et al. 2014; Lee & Chiang 2015), as well as hydrodynamical interactions between the envelope of the embedded protoplanet and its disk that also slow cooling (Ormel et al. 2015a, 2015b; Lee 2019; Ali-Dib et al. 2020). Another potential solution is formation via high-impact protoplanet collisions that remove initial gas atmospheres (Inamdar & Schlichting 2015; Biersteker & Schlichting 2019), leaving the final accretion to occur in a gas-depleted environment.

5.5. Influence of Atmospheric Metallicity

Our models of the planetary atmospheric envelopes assumed solar metallicities. However, enhanced metallicities have been inferred for many close-in planets ranging from Neptune to Jupiter mass scales (e.g., Morley et al. 2017; Spake et al. 2019). The increased opacity at high metallicity results in the

radiative-convective boundary moving upward in the atmosphere to lower pressures (Thorngren et al. 2019), thereby widening the convective zone. This increases the efficiency of tidal heating, such that the radius inflation is more extreme for the same amount of heating. Examining representative case studies with our MESA model, we confirmed that a larger atmospheric metallicity results in both a larger radius and a larger degree of radius inflation for a given f_{env} and L_{tide} . Accordingly, if most sub-Saturns have enhanced atmospheric metallicities, then they are even more affected by tidal heating than our calculations indicate.

5.6. Predictions and Observational Signatures

If many sub-Saturns are in fact less envelope-rich than they appear when ignoring tides, we predict that planets with $f_{\text{env}} \sim 50\%$ should not exist (or at least, should be exceedingly rare) on distant orbits where tidal heating is weak, specifically beyond ~ 100 days. Moreover, unlike the radius occurrence rate distribution, which appears flat beyond $\sim 4 R_{\oplus}$, there may be a gap in the distribution of f_{env} between the primary group of relatively gas-poor sub-Neptune/sub-Saturns with $f_{\text{env}} \lesssim 10\%–20\%$ and the gas giant group with $f_{\text{env}} > 100\%$.

In terms of direct observations, the tidal heating in some hot sub-Saturns may exhibit signatures that are potentially observable, particularly with the James Webb Space Telescope (Gardner et al. 2006). Tidal heating changes the temperature and chemistry of a planet’s deep interior and can result in deviations of its emission spectrum, as demonstrated for GJ 436 b by Morley et al. (2017). Moreover, tidal heating might be observable in full-orbit photometric phase curves through perturbations to the day–night temperature contrasts, since tidal heating is more longitudinally uniform than stellar insolation. Further modeling work is necessary to investigate this in detail. Finally, signatures of nonzero obliquities, which can induce obliquity tides, can be probed by phase curve modeling (Adams et al. 2019) and secondary eclipse mapping (Rauscher 2017).

6. Summary

Many sub-Saturns have such large radii and low masses that standard core-envelope structural models have suggested that they must have massive atmospheric envelopes comprising $\sim 50\%$ of their total mass (e.g., Petigura et al. 2018a, 2020; Addison et al. 2020). This posed a problem for the theory of core accretion, which dictates that planets undergo runaway gas accretion when their envelope mass reaches their core mass. These 50/50 core/envelope planets, however, are generally found on short-period orbits with non-negligible eccentricities. Accordingly, tidal heating from eccentricity tides (as well as potential obliquity tides) is substantial, and this heating generates atmospheric inflation. When this effect is ignored, the atmospheres can appear much more massive than they actually are.

Beginning with a case study of the K2-19 system,¹¹ we showed that heating from tidal dissipation can resolve the apparent structural problems. K2-19 b’s envelope mass fraction estimate is $f_{\text{env,t}} \approx 5\%–20\%$ when tides are included in the model, rather than the $f_{\text{env,0}} \approx 50\%$ previously thought. Within the broader population of sub-Saturns, estimates of their envelope mass

fractions are smaller than previously thought by an average of $\langle f_{\text{env,0}} - f_{\text{env,t}} \rangle = 10\%$. Nearly half of these planets would have radii consistent with the sub-Neptune population if they were not tidally inflated. Thus, a short-period planet’s core mass and envelope mass fraction—rather than its radius, which is dependent on its dynamical state through tidal inflation—are more fundamental tracers of the planet formation process. Further demographic and modeling studies are required to examine these properties across the planet population.

We are grateful to the anonymous referee for the helpful comments and suggestions. We thank Chris Spalding for insightful conversations. We also thank Howard Chen & Leslie Rogers for their publicly available MESA model. S.M. is supported by the NSF Graduate Research Fellowship Program under Grant DGE-1122492. E.P. acknowledges the generous support of the Alfred P. Sloan Foundation. K.B. is grateful to the David and Lucile Packard Foundation and the Alfred P. Sloan Foundation for their generous support. This research has made use of the NASA Exoplanet Archive, which is operated by the California Institute of Technology, under contract with the National Aeronautics and Space Administration under the Exoplanet Exploration Program.

Appendix

Obliquity Excitation from Secular Spin–Orbit Resonance

In Section 3, we showed that inferences of the envelope mass fractions of the K2-19 planets are significantly impacted after accounting for tidal inflation from eccentricity and/or obliquity tides. The eccentricities are measured to be $e \sim 0.2$ for both K2-19 b and K2-19 c, but their obliquities are unknown. The K2-19 planets may have nonzero obliquities if they are trapped in secular spin–orbit resonances, dynamical configurations that involve a commensurability between the frequencies of the planet’s spin-axis precession and orbital precession. Encounters with these resonances lead planets to reach high obliquities. The mechanism is responsible for the obliquity excitations of several solar system planets (e.g., Laskar & Robutel 1993; Touma & Wisdom 1993; Ward & Hamilton 2004; Ward & Canup 2006), and it has recently been studied in the context of short-period exoplanetary systems (e.g., Millholland & Laughlin 2018, 2019). In particular, Millholland & Laughlin (2019) showed that planets in short-period, compact, multiplanet systems are intrinsically susceptible to these obliquity-exciting resonances due to a proximity between their spin and orbital precession frequencies. Since K2-19 is one such compact multiplanet system, its planets may have enhanced obliquities. To examine this explicitly, here we will calculate the system’s precession frequencies and explore their plausible evolutionary history.

We begin by defining the relevant frequencies of precession of the planets’ spin axes and orbits. Planetary spin axis precession arises in response to the torque induced by the host star onto the rotationally flattened figure of the planet. The precession period is equal to $T_{\alpha} = 2\pi/(\alpha \cos \epsilon)$, where α is called the precession constant. In the absence of satellites, α is given by (Neron de Surgy & Laskar 1997; Correia et al. 2003)

$$\alpha = \frac{1}{2} \frac{M_{\star}}{M_p} \left(\frac{R_p}{a} \right)^3 \frac{k_2}{C} \frac{\omega}{(1 - e^2)^{3/2}}. \quad (\text{A1})$$

In addition to the variables defined earlier in Section 2.1, C is the planet’s moment of inertia normalized by $M_p R_p^2$. We may

¹¹ Our analysis for K2-19 b, along with a condensed data set of the MESA simulations and our general procedure for estimating envelope fractions, is provided at <https://github.com/smllholland/Sub-Saturns/>.

assume that short-period planets have reached their equilibrium spin rotation rate (Equation (6)).

The second relevant precessional motion is the orbit nodal regression, defined with a frequency $g = \dot{\Omega}$, where Ω is the longitude of ascending node. Nodal recession may be induced by a variety of sources (in general, any deviation from a $1/r$ potential). Here, we consider the case that it is driven by secular planet–planet interactions. To be explicit, we delineate the example of an isolated two-planet interaction, but the full Laplace–Lagrange secular solution must be used to capture the dynamics of multiplanet systems. When eccentricities and inclinations are small, the longitudes of ascending node of two planets not near mean-motion resonances will regress uniformly at a frequency (Murray & Dermott 1999)

$$g_{\text{LL}} = -\frac{1}{4}b_{3/2}^{(1)}(\alpha_{ij})\alpha_{ij}\left(n_i\frac{M_{pj}}{M_\star + M_{pj}}\alpha_{ij} + n_j\frac{M_{pi}}{M_\star + M_{pi}}\right). \quad (\text{A2})$$

Here, the subscript LL stands for Laplace–Lagrange. In addition, $\alpha_{ij} = a_i/a_j$, and we use the subscripts i and j to refer to a pair of planets with planet i the interior of the two. The constant, $b_{3/2}^{(1)}(\alpha_{ij})$, is a Laplace coefficient, defined by

$$b_{3/2}^{(1)}(\alpha_{ij}) = \frac{1}{\pi} \int_0^{2\pi} \frac{\cos \psi}{(1 - 2\alpha_{ij} \cos \psi + \alpha_{ij}^2)^{3/2}} d\psi. \quad (\text{A3})$$

Before proceeding, we briefly note two modifications to g_{LL} . First, if the planets are near MMR, as the K2-19 planets are, the nodal recession frequency is smaller by a factor of $g/g_{\text{LL}} \sim 0.5$, which depends on the eccentricities and libration amplitude (Sansottera & Libert 2019). Second, in systems with more than two planets, the orbits will not precess uniformly; instead, they will have several eigenfrequency modes within their perturbations. The secular spin–orbit resonance may arise as a commensurability between the spin axis precession frequency and any one of these secular eigenfrequencies (e.g., Ward & Hamilton 2004).

A secular spin–orbit resonance is a particular case of a more general phenomenon called a ‘‘Cassini state,’’ an equilibrium configuration of the planet’s spin vector in the precessing orbital frame. There are up to four Cassini states depending on the value of the ratio g/α . For a given set of frequencies, g and α , and a given orbital inclination with respect to the invariable plane, I , the equilibrium solutions of the planet obliquity satisfy

$$g \sin(\epsilon - I) + \alpha \cos \epsilon \sin \epsilon = 0. \quad (\text{A4})$$

When $I \ll \epsilon$, this criterion simplifies to

$$|g| \approx \alpha \cos \epsilon. \quad (\text{A5})$$

This simplification is appropriate for the case under consideration here, given the sub-degree mutual inclinations of the planetary orbits (see Table 2).

In order to calculate the resonant obliquity—specifically, the stable equilibrium obliquity in Cassini state 2—we can combine Equations (6) and (A5) and solve for the obliquity. The result is

$$\cos \epsilon = \left[2 \frac{N(e)}{\Omega(e)} \frac{\alpha_{\text{syn}}}{|g|} - 1 \right]^{-\frac{1}{2}}, \quad (\text{A6})$$

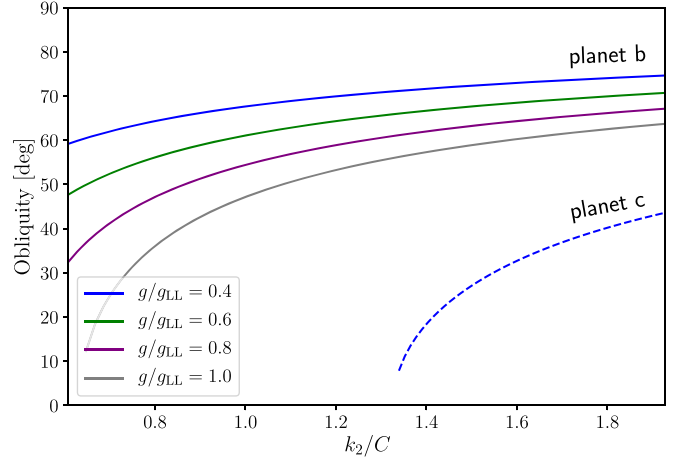


Figure A1. Resonant equilibrium obliquity (Equation (A6)) for K2-19 b (solid lines) and K2-19 c (dashed lines) as a function of k_2/C and for different values of g/g_{LL} . A high obliquity resonance for planet b is robust across a range of parameter space; the resonance is possible for planet c but less likely.

where $\alpha_{\text{syn}} = \alpha(n/\omega)$ is the spin precession constant in the case of synchronous rotation with $\omega = n$. To be clear, this expression yields the obliquity the planet would have if it is resonant, but this resonance locking is not guaranteed.

We use Equation (A6) to determine whether the K2-19 planets could plausibly have excited obliquities due to their participation in secular spin–orbit resonances. All parameters involved in this calculation have been constrained (and are listed in Table 2), with the exception of the values of k_2 and C . We assume fiducial values as follows. Based on estimates (Lainey 2016) of the Love numbers for Saturn ($k_2 = 0.39$), Uranus ($k_2 = 0.104$), and Neptune ($k_2 = 0.127$), we consider a broad range of values, $k_2 \in [0.1, 0.5]$. Next, we calculate C by making use of the Radau–Darwin relationship (Hubbard 1984; Kramm et al. 2011), which relates the nondimensional moment of inertia to the first-order response to tidal distortion,

$$C_{\text{rd}} = \frac{2}{3} \left[1 - \frac{2}{5} \left(\frac{5}{k_2 + 1} - 1 \right)^{\frac{1}{2}} \right]. \quad (\text{A7})$$

Figure A1 shows curves of the resonant obliquities for planets b and c as a function of k_2/C and g/g_{LL} . This latter quantity determines the degree to which the nodal recession frequency deviates from the Laplace–Lagrange value. We see that planet b could quite easily be in secular spin–orbit resonance; that is, its resonant obliquity is well-defined for a wide range of k_2/C and g/g_{LL} . Planet c could also have a resonantly enhanced obliquity, but that is less likely, as it would require a relatively small value of g/g_{LL} and $k_2/C \gtrsim 0.4$.

We can make this argument more explicit by showing a plausible example of the system’s evolutionary history. To do this, we apply a gravitational N -body code that models the planetary tidal, spin, and orbital evolution. This is a direct numerical integration (as opposed to a secular calculation) adopted from the framework of Mardling & Lin (2002). We account for accelerations due to tides raised on the planets from the host star using equilibrium tide theory in the viscous approximation, and we include the accelerations on the planets from the star’s quadrupole gravitational potential. The details of the code are provided in Section 1.2 of the Methods of Millholland & Laughlin (2019).

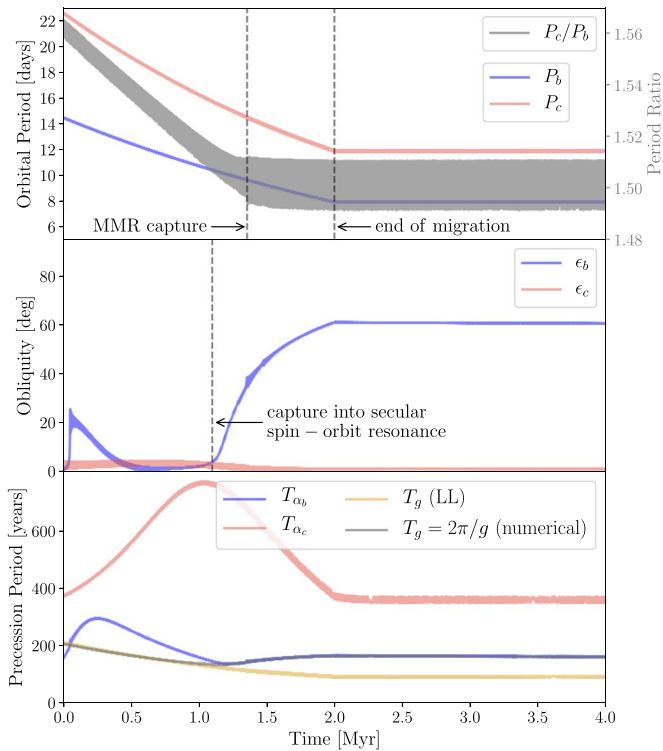


Figure A2. Example dynamical evolution of the K2-19 system while planets b and c undergo convergent inward migration for the first 2 Myr. Top panel: evolution of the orbital periods and period ratio; the 3:2 MMR is capture at ~ 1.3 Myr, and the migration ends at 2 Myr. Middle panel: evolution of the obliquities of planets b and c. Bottom panel: evolution of the spin and orbital precession periods. Blue and red curves show the precession periods of the spin axes of planets b and c, respectively. Gray curve shows the orbit nodal recession period, which increases away from the Laplace–Lagrange secular solution in yellow as the system enters the MMR.

The basic setup of our simulation consists of the K2-19 host star and planets b and c, with all bodies endowed with structure. We assign fiducial values, $k_{2,b} = k_{2,c} = 0.3$, $C_b = C_c = 0.3$, and $Q_b = Q_c = 10^4$. We set the initial rotation periods to reflect partial but incomplete spin-down, $P_{rot,b} = 5$ days and $P_{rot,c} = 3$ days. Finally, we initialize the planets on apsidally aligned orbits with initial eccentricities, $e_1 = e_2 = 0.15$. While the details of the resulting evolution depend somewhat on these initial conditions, the primary features of the response are generalizable.

If the outer planets in the K2-19 system are indeed locked into a mean motion resonance, they must have experienced slow convergent migration. Accordingly, we assume that planets b and c initially start slightly wide of a 3:2 period ratio and migrate inward convergently due to (unmodeled) interactions with the protostellar disk. We set the migration timescales equal to $\tau_{a_b} = a_b/a_b = 5$ Myr and $\tau_{a_c} = \tau_{a_b}/1.1$, and the setup is such that the planets capture the MMR at ~ 1.3 Myr and reach their present-day semimajor axes after 2 Myr. The longitudes of perihelion are locked into libration about $\Delta\varpi \approx 0$, in accordance with the observed apsidal alignment of the system.

The resulting dynamical evolution is displayed in Figure A2. Planet b first encounters the secular spin–orbit resonance at ~ 1.1 Myr when T_{α}/T_g crosses unity from below, producing a resonant kick of the obliquity to $\sim 20^\circ$. Shortly thereafter, planet b encounters the resonance again, this time T_{α}/T_g reaching unity from above and resulting in a resonant capture.

The planet’s obliquity reaches 60° by the end of the migration at 2 Myr. While planet b’s obliquity is readily excited by the resonant interactions, planet c does not encounter the resonance in this example. This is consistent with the constraints indicated in Figure A1.

ORCID iDs

Sarah Millholland <https://orcid.org/0000-0003-3130-2282>

Erik Petigura <https://orcid.org/0000-0003-0967-2893>

Konstantin Batygin <https://orcid.org/0000-0002-7094-7908>

References

- Adams, A. D., Millholland, S., & Laughlin, G. P. 2019, *AJ*, 158, 108
- Addison, B. C., Wright, D. J., Nicholson, B. A., et al. 2020, arXiv:2001.07345
- Akeson, R. L., Chen, X., Ciardi, D., et al. 2013, *PASP*, 125, 989
- Ali-Dib, M., Cumming, A., & Lin, D. N. C. 2020, *MNRAS*, 494, 2440
- Anderson, D. R., Collier Cameron, A., Delrez, L., et al. 2017, *A&A*, 604, A110
- Barragán, O., Grziwa, S., Gandolfi, D., et al. 2016, *AJ*, 152, 193
- Barros, S. C. C., Gosselin, H., Lillo-Box, J., et al. 2017, *A&A*, 608, A25
- Batygin, K., Bodenheimer, P. H., & Laughlin, G. P. 2016, *ApJ*, 829, 114
- Batygin, K., & Morbidelli, A. 2013, *A&A*, 556, A28
- Batygin, K., Stevenson, D. J., & Bodenheimer, P. H. 2011, *ApJ*, 738, 1
- Biersteker, J. B., & Schlichting, H. E. 2019, *MNRAS*, 485, 4454
- Bodenheimer, P., Laughlin, G., & Lin, D. N. C. 2003, *ApJ*, 592, 555
- Bodenheimer, P., Lin, D. N. C., & Mardling, R. A. 2001, *ApJ*, 548, 466
- Boué, G., Correia, A. C. M., & Laskar, J. 2016, *CeMDA*, 126, 31
- Brady, M. T., Petigura, E. A., Knutson, H. A., et al. 2018, *AJ*, 156, 147
- Carleo, I., Gandolfi, D., Barragán, O., et al. 2020, arXiv:2004.10095
- Chen, H., & Rogers, L. A. 2016, *ApJ*, 831, 180
- Cochran, W. D., Fabrycky, D. C., Torres, G., et al. 2011, *ApJS*, 197, 7
- Correia, A. C. M., Boué, G., Laskar, J., & Rodríguez, A. 2014, *A&A*, 571, A50
- Correia, A. C. M., Laskar, J., & de Surgy, O. N. 2003, *Icar*, 163, 1
- Cui, X.-Q., Zhao, Y.-H., Chu, Y.-Q., et al. 2012, *RAA*, 12, 1197
- Darwin, G. H. 1880, *RSPT*, 171, 713
- Demangeon, O. D. S., Faedi, F., Hébrard, G., et al. 2018, *A&A*, 610, A63
- Dressing, C. D., & Charbonneau, D. 2013, *ApJ*, 767, 95
- Efroimsky, M., & Williams, J. G. 2009, *CeMDA*, 104, 257
- Esposito, M., Armstrong, D. J., Gandolfi, D., et al. 2019, *A&A*, 623, A165
- Ferraz-Mello, S. 2013, *CeMDA*, 116, 109
- Ferraz-Mello, S., Rodríguez, A., & Hussmann, H. 2008, *CeMDA*, 101, 171
- Foreman-Mackey, D., Hogg, D. W., Lang, D., & Goodman, J. 2013, *PASP*, 125, 306
- Fressin, F., Torres, G., Charbonneau, D., et al. 2013, *ApJ*, 766, 81
- Freudenthal, J., von Essen, C., Ofir, A., et al. 2019, *A&A*, 628, A108
- Fulton, B. J., & Petigura, E. A. 2018, *AJ*, 156, 264
- Fulton, B. J., Petigura, E. A., Howard, A. W., et al. 2017, *AJ*, 154, 109
- Gaia Collaboration, Brown, A. G. A., Vallenari, A., et al. 2018, *A&A*, 616, A1
- Gao, P., & Zhang, X. 2020, *ApJ*, 890, 93
- Gardner, J. P., Mather, J. C., Clampin, M., et al. 2006, *SSRv*, 123, 485
- Gavrilov, S. V., & Zharkov, V. N. 1977, *Icar*, 32, 443
- Gelman, A., & Rubin, D. B. 1992, *StatSci*, 7, 457
- Ginzburg, S., & Sari, R. 2017, *MNRAS*, 464, 3937
- Ginzburg, S., Schlichting, H. E., & Sari, R. 2016, *ApJ*, 825, 29
- Ginzburg, S., Schlichting, H. E., & Sari, R. 2018, *MNRAS*, 476, 759
- Goldreich, P., & Soter, S. 1966, *Icar*, 5, 375
- Goodman, J., & Weare, J. 2010, *Communications in Applied Mathematics and Computational Science*, 5, 65
- Hadden, S., & Lithwick, Y. 2014, *ApJ*, 787, 80
- Hadden, S., & Lithwick, Y. 2017, *AJ*, 154, 5
- Hardegree-Ullman, K. K., Zink, J. K., Christiansen, J. L., et al. 2020, *ApJS*, 247, 28
- Hartman, J. D., Bakos, G. Á., Kipping, D. M., et al. 2011, *ApJ*, 728, 138
- Heller, R., Rodenbeck, K., & Hippke, M. 2019, *A&A*, 625, A31
- Hellier, C., Anderson, D. R., Triard, A. H. M. J., et al. 2019, *MNRAS*, 488, 3067
- Howard, A. W., Marcy, G. W., Bryson, S. T., et al. 2012, *ApJS*, 201, 15
- Hsu, D. C., Ford, E. B., Ragozzine, D., & Ashby, K. 2019, *AJ*, 158, 109
- Hubbard, W. B. 1984, *Planetary Interiors* (New York: Van Nostrand Reinhold)
- Huber, D., Carter, J. A., Barbieri, M., et al. 2013, *Sci*, 342, 331
- Hubickyj, O., Bodenheimer, P., & Lissauer, J. J. 2005, *Icar*, 179, 415
- Hut, P. 1981, *A&A*, 99, 126
- Ibgui, L., & Burrows, A. 2009, *ApJ*, 700, 1921

- Inamdar, N. K., & Schlichting, H. E. 2015, *MNRAS*, **448**, 1751
- Jackson, B., Greenberg, R., & Barnes, R. 2008, *ApJ*, **681**, 1631
- Johnson, J. A., Petigura, E. A., Fulton, B. J., et al. 2017, *AJ*, **154**, 108
- Jontof-Hutter, D., Lissauer, J. J., Rowe, J. F., & Fabrycky, D. C. 2014, *ApJ*, **785**, 15
- Komacek, T. D., & Youdin, A. N. 2017, *ApJ*, **844**, 94
- Kramm, U., Nettelmann, N., Redmer, R., & Stevenson, D. J. 2011, *A&A*, **528**, A18
- Lainey, V. 2016, *CeMDA*, **126**, 145
- Laskar, J., & Robutel, P. 1993, *Natur*, **361**, 608
- Leconte, J., Chabrier, G., Baraffe, I., & Levrard, B. 2010, *A&A*, **516**, A64
- Lee, E. J. 2019, *ApJ*, **878**, 36
- Lee, E. J., & Chiang, E. 2015, *ApJ*, **811**, 41
- Lee, E. J., Chiang, E., & Ormel, C. W. 2014, *ApJ*, **797**, 95
- Libby-Roberts, J. E., Berta-Thompson, Z. K., Désert, J.-M., et al. 2020, *AJ*, **159**, 57
- Lissauer, J. J., Jontof-Hutter, D., Rowe, J. F., et al. 2013, *ApJ*, **770**, 131
- Lissauer, J. J., Marcy, G. W., Rowe, J. F., et al. 2012, *ApJ*, **750**, 112
- Livingston, J. H., Crossfield, I. J. M., Petigura, E. A., et al. 2018, *AJ*, **156**, 277
- Lopez, E. D., & Fortney, J. J. 2014, *ApJ*, **792**, 1
- Maciejewski, G., Niedzielski, A., Nowak, G., et al. 2014, *AcA*, **64**, 323
- Marcy, G. W., Isaacson, H., Howard, A. W., et al. 2014, *ApJS*, **210**, 20
- Mardling, R. A., & Lin, D. N. C. 2002, *ApJ*, **573**, 829
- Mignard, F. 1979, *M&P*, **20**, 301
- Miller, N., Fortney, J. J., & Jackson, B. 2009, *ApJ*, **702**, 1413
- Millholland, S. 2019, *ApJ*, **886**, 72
- Millholland, S., & Laughlin, G. 2018, *ApJL*, **869**, L15
- Millholland, S., & Laughlin, G. 2019, *NatAs*, **3**, 424
- Mills, S. M., Fabrycky, D. C., Migaszewski, C., et al. 2016, *Natur*, **533**, 509
- Mills, S. M., Howard, A. W., Weiss, L. M., et al. 2019, *AJ*, **157**, 145
- Mizuno, H. 1980, *PThPh*, **64**, 544
- Morley, C. V., Knutson, H., Line, M., et al. 2017, *AJ*, **153**, 86
- Murray, C. D., & Dermott, S. F. 1999, *Solar System Dynamics* (Cambridge: Cambridge Univ. Press)
- Neron de Surgy, O., & Laskar, J. 1997, *A&A*, **318**, 975
- Ofir, A., Dreizler, S., Zechmeister, M., & Husser, T.-O. 2014, *A&A*, **561**, A103
- Ogilvie, G. I., & Lin, D. N. C. 2004, *ApJ*, **610**, 477
- Ormel, C. W., Kuiper, R., & Shi, J.-M. 2015a, *MNRAS*, **446**, 1026
- Ormel, C. W., Shi, J.-M., & Kuiper, R. 2015b, *MNRAS*, **447**, 3512
- Owen, J. E., & Wu, Y. 2017, *ApJ*, **847**, 29
- Paxton, B., Bildsten, L., Dotter, A., et al. 2011, *ApJS*, **192**, 3
- Paxton, B., Cantiello, M., Arras, P., et al. 2013, *ApJS*, **208**, 4
- Paxton, B., Marchant, P., Schwab, J., et al. 2015, *ApJS*, **220**, 15
- Paxton, B., Schwab, J., Bauer, E. B., et al. 2018, *ApJS*, **234**, 34
- Petigura, E. A., Benneke, B., Batygin, K., et al. 2018a, *AJ*, **156**, 89
- Petigura, E. A., Howard, A. W., & Marcy, G. W. 2013, *PNAS*, **110**, 19273
- Petigura, E. A., Howard, A. W., Marcy, G. W., et al. 2017a, *AJ*, **154**, 107
- Petigura, E. A., Livingston, J., Batygin, K., et al. 2020, *AJ*, **159**, 2
- Petigura, E. A., Marcy, G. W., Winn, J. N., et al. 2018b, *AJ*, **155**, 89
- Petigura, E. A., Sinukoff, E., Lopez, E. D., et al. 2017b, *AJ*, **153**, 142
- Petit, A. C., Petigura, E. A., Davies, M. B., & Johansen, A. 2020, arXiv:2003.04931
- Piaulet, C., Benneke, B., Rubenzahl, R., et al. 2019, AAS/Division for Extreme Solar Systems Abstracts, 51, 102.04
- Pollack, J. B., Hubickyj, O., Bodenheimer, P., et al. 1996, *Icar*, **124**, 62
- Puranam, A., & Batygin, K. 2018, *AJ*, **155**, 157
- Rauscher, E. 2017, *ApJ*, **846**, 69
- Rogers, L. A. 2015, *ApJ*, **801**, 41
- Rogers, L. A., & Seager, S. 2010, *ApJ*, **712**, 974
- Rowe, J. F., Bryson, S. T., Marcy, G. W., et al. 2014, *ApJ*, **784**, 45
- Sansottera, M., & Libert, A. S. 2019, *CeMDA*, **131**, 38
- Spake, J. J., Sing, D. K., Wakeford, H. R., et al. 2019, arXiv:1911.08859
- Spiegel, D. S., & Burrows, A. 2013, *ApJ*, **772**, 76
- Stassun, K. G., Collins, K. A., & Gaudi, B. S. 2017, *AJ*, **153**, 136
- Stevenson, D. J. 1982, *P&SS*, **30**, 755
- Storch, N. I., & Lai, D. 2014, *MNRAS*, **438**, 1526
- Storch, N. I., & Lai, D. 2015, *MNRAS*, **450**, 3952
- Sun, L., Ioannidis, P., Gu, S., et al. 2019, *A&A*, **624**, A15
- Thorngren, D., Gao, P., & Fortney, J. J. 2019, *ApJL*, **884**, L6
- Tittlemore, W. C., & Wisdom, J. 1989, *Icar*, **78**, 63
- Touma, J., & Wisdom, J. 1993, *Sci*, **259**, 1294
- Wang, L., & Dai, F. 2019, *ApJL*, **873**, L1
- Ward, W. R., & Canup, R. M. 2006, *ApJL*, **640**, L91
- Ward, W. R., & Hamilton, D. P. 2004, *AJ*, **128**, 2501
- Weiss, L. M., & Marcy, G. W. 2014, *ApJL*, **783**, L6
- Wisdom, J. 2008, *Icar*, **193**, 637
- Wolfgang, A., & Lopez, E. 2015, *ApJ*, **806**, 183
- Yee, S. W., Petigura, E. A., Fulton, B. J., et al. 2018, *AJ*, **155**, 255
- Yu, L., Rodriguez, J. E., Eastman, J. D., et al. 2018, *AJ*, **156**, 127
- Zhang, K., & Hamilton, D. P. 2008, *Icar*, **193**, 267